Journal of
Composites Science

MDPI

Article

Study on Low-Velocity Impact Resistance of SMA-CFRP U-Shaped Structure Considering Curing Residual Stress

Liangdi Wang [1,2], Yingjie Xu [1,2,*], Jun Wang [2,3,*] and Shengnan Zhang [1,4]

[1] School of Mechanical Engineering, Northwestern Polytechnical University, Xi'an 710072, China; wld@mail.nwpu.edu.cn (L.W.); zhang.shengnan@mail.nwpu.edu.cn (S.Z.)
[2] Shaanxi Province Key Laboratory of Aeronautical and Aerospace Structure Technology, Northwestern Polytechnical University, Xi'an 710072, China
[3] Unmanned System Research Institute, Northwestern Polytechnical University, Xi'an 710072, China
[4] Department of Mechanical Engineering, National University of Singapore, Singapore 117575, Singapore
* Correspondence: xu.yingjie@nwpu.edu.cn (Y.X.); wang.jun@nwpu.edu.cn (J.W.)

Abstract

While carbon fiber-reinforced polymer (CFRP) composites are widely utilized in aerospace applications due to their exceptional specific strength and stiffness, they are inevitably subjected to impact loads during service, which can easily induce internal damage such as delamination. To mitigate these issues, this study investigates the low-velocity impact behavior of an SMA-reinforced CFRP U-shaped structure, emphasizing the critical role of curing-induced residual stresses. A numerical model incorporating the thermal-mechanical manufacturing history was developed and validated against experimental data. Results indicate that while embedded superelastic SMA wires effectively suppress crack propagation and enhance energy absorption, neglecting residual stresses leads to a significant overestimation of structural rigidity and peak loads. Due to the coefficient of thermal expansion mismatch between the SMA wires and the resin matrix, the SMA-CFRP system exhibits higher sensitivity to initial internal stresses than pure CFRP. By accounting for the residual stress field, the relative error in predicted peak force and absorbed energy for the SMA-CFRP model was reduced from 9.3% to 3.5% and 18.9% to 7.8%, respectively. These findings demonstrate that residual stress lowers the failure threshold and is essential for capturing the synergistic effects of SMA phase transformation and matrix damage, providing a more accurate reconstruction of the structural energy balance.

Keywords: carbon fiber-reinforced polymer; shape memory alloy; U-shaped structure; curing residual stress; low-velocity impact

Check for updates

Academic Editor: Marco Montemurro

Received: 30 March 2026
Revised: 20 April 2026
Accepted: 24 April 2026
Published: 27 April 2026

Copyright: © 2026 by the authors. Licensee MDPI, Basel, Switzerland. This article is an open access article distributed under the terms and conditions of the Creative Commons Attribution (CC BY) license.

1. Introduction

Advanced composites, spearheaded by continuous carbon fiber-reinforced polymers (CFRPs), represent a cornerstone for structural lightweighting in aerospace and high-end engineering, credited to their unrivaled specific mechanical properties and tailorable architectures. U-shaped geometries serve as indispensable load-bearing elements in vital aerospace assemblies, including wing leading edges and empennages. Nevertheless, these components are frequently exposed to low-velocity impact (LVI) events, such as runway debris strikes and avian ingestions, during critical operational phases. Addressing the trade-off between maintaining high specific strength and simultaneously bolstering impact resilience and damage tolerance is thus a pressing scientific priority in contemporary materials research.

Conventional methodologies for bolstering the delamination resistance of polymer matrix composites have predominantly relied on architectural toughening techniques, including stitching [1], 3D weaving [2], and Z-pin reinforcement [3]. Recently, shape memory alloy (SMA) integration strategies have emerged as a compelling alternative, distinguished by their unique functional mechanisms. Leveraging superelasticity with reversible strains reaching up to 8% [4], significant hysteretic behavior, and exceptional energy dissipation [5], SMAs provide composites with enhanced damping capabilities, robust damage tolerance, and the potential for active structural reconfiguration [6]. These multi-functional characteristics represent a significant technological leap over traditional reinforcement paradigms.

Despite these advantages, the incorporation of SMAs into CFRP architectures introduces formidable challenges, particularly regarding the interfacial compatibility between the SMA and the polymer matrix—a factor that remains a pivotal bottleneck for industrial-scale applications. In large-scale and complex CFRP components, thermal gradients between the prepreg layers and the tooling during curing inevitably trigger residual stress accumulation [7,8]. The integration of SMA wires further complicates this issue; due to the pronounced mismatch in the Coefficient of Thermal Expansion (CTE), their presence exacerbates local fiber distortions and engenders severe stress concentrations and suboptimal bonding at the interface [9]. These deleterious effects ultimately diminish the intended mechanical reinforcement of the hybrid composite.

Current research on the mechanical properties of SMA-reinforced composites primarily focuses on three thematic areas: process parameter optimization, interfacial effect regulation, and crack-healing mechanisms [10,11].

Initially, the influence of material and processing parameters on mechanical performance has been extensively scrutinized, specifically regarding key factors such as SMA wire diameter, pre-strain magnitude, embedding location, and orientation. For instance, Fallah [12] investigated the nonlinear dynamic response of micro-SMA composite plates and observed that increasing the wire diameter enhances the damping ratio. Furthermore, Jang et al. [13] elucidated a negative correlation between carbon fiber ply angles and tensile strength, noting a significant degradation in strength as the orientation angle increased from 0° to 90°.

Notably, the impact of these parameters is frequently coupled with interfacial phenomena. Zhao et al. [14] identified that the SMA/resin interfacial bonding performance is the determining factor for the static and dynamic properties of laminates; they successfully enhanced this interfacial strength through the incorporation of nanoparticles. The significance of interfacial modification was further validated by Wang et al. [15], who demonstrated that SMA fibers treated with a KH550 coupling agent significantly bolster the overall mechanical performance of the composite.

Building upon the optimization of parameters and interfaces, the active actuation characteristics of SMAs have introduced innovative paradigms for crack healing. The Cohades [16] group utilized thermally actuated SMA wires to close longitudinal cracks in epoxy-polycaprolactone-based composites via the mechanical bridging effect. Finally, Karimi et al. [17] employed an extended finite element model (XFEM) to achieve the first numerical simulation of mixed-mode crack propagation and subsequent healing, providing a robust theoretical framework for the damage remediation mechanisms in SMA-enhanced composites.

Current research on the curing deformation of composite materials primarily revolves around the influence of mechanisms of residual stress, deformation control methodologies, and process optimization strategies. At the mechanistic level, the coupled effect of curing residual stress and thermal stress not only induces mechanical property degradation,

such as reduced structural stiffness [18] and interlaminar delamination, but also leads to dimensional stability issues, including warping deformation [19] and the superposition of assembly stresses [20]. Furthermore, these factors may accelerate creep and fatigue crack propagation during long-term service.

Paulo et al. [21] developed a Representative Volume Element (RVE) model to simulate the thermal curing process and analyzed the impact of micro-residual stresses on the mechanical properties of unidirectional CFRP prepregs. Their results showed a 10% reduction in transverse strength, with little effect on elastic properties. Zhang et al. [22] used a multiscale approach to study the evolution of micro-curing residual stresses and their effects on the out-of-plane tensile properties of T700/7901 composites, finding that residual stresses delayed interfacial damage and matrix plastic deformation.

Compared to traditional flat configurations, U-shaped composite structures face more severe internal challenges during the curing process due to the introduction of complex curved geometries [23]. During the thermo-mechanical coupling cycles, anisotropic shrinkage differentials are highly likely to occur within the curved regions, leading to significant residual stress accumulation and geometric distortions such as spring-back or warping [24]. Given that resin-based composites inherently exhibit distinct interlaminar brittleness, these pre-existing initial residual stress fields often generate nonlinear superposition effects with external impact loads encountered during service. This stress coupling not only triggers the premature initiation of interfacial micro-cracks but also accelerates delamination propagation and matrix fragmentation during the impact energy release process, thereby significantly exacerbating the structural damage evolution and weakening the residual strength.

Based on the current research, although SMA has been widely used to enhance the mechanical properties and impact resistance of CFRP, most studies focus on flat panels, with limited attention to U-shaped components. Furthermore, previous research has primarily concentrated on SMA material parameters, interface effects, and crack healing, with little focus on the residual stress generated during the curing process of SMA-enhanced CFRP and its impact on mechanical behavior. This study innovatively incorporates curing deformation into the mechanical analysis of SMA-enhanced CFRP, exploring the impact of curing residual stress on low-velocity impact performance, and validating the model through experiments to fill the gaps in existing research and provide new theoretical insights for optimizing SMA-enhanced composite design and applications.

2. Materials and Methods

2.1. Modeling Methodology

In this work, T700/H69 carbon/epoxy prepreg was used to manufacture CFRP and SMA-CFRP U-shaped leading-edge specimens by autoclave molding. The curing-induced warpage was measured experimentally and compared with the numerical results for validation. The residual stress field obtained from the thermo-mechanically coupled curing analysis was then transferred to the subsequent low-velocity impact model as the initial stress state, and the predicted impact responses were further verified against the experimental data.

2.1.1. Cure Reaction Kinetics Equation

Differential Scanning Calorimetry (DSC) was employed to characterize the curing behavior of the H69 epoxy resin, and the corresponding cure kinetics were represented by an autocatalytic Equation [25].

$$\begin{aligned} d\alpha/dt &= K\alpha^m(1-\alpha)^n \\ K &= Aexp(-\Delta E/RT) \end{aligned} \quad (1)$$

Here, K denotes the reaction rate constant, α is the degree of cure, t is time, and T is temperature. A, ΔE, and R represent the pre-exponential factor, activation energy, and universal gas constant, respectively, while m and n are the kinetic exponents. These parameters were identified by fitting the DSC data, as listed in Table 1 [26]. Owing to the small thickness of the laminates and the embedded SMA wire configuration, the temperature gradient through the structure was neglected in the present analysis.

Table 1. Curing kinetic parameters of H69 resin.

Parameters	Values
Pre-exponential factor	$A = 3.4 \times 10^8\ s^{-1}$
Activation energy	$\Delta E = 83,256.4\ J/mol$
Kinetic exponents	$m = 0.69$
	$n = 2.11$

As curing proceeds, the resin gradually transforms from a viscous state to a glassy solid. Accordingly, the elastic modulus E_r and Poisson's ratio v_r of the resin are expressed as follows [25]:

$$E_r = \begin{cases} E_r^0, & \alpha < \alpha_{gel} \\ (1-\alpha_{mod})E_r^0 + \alpha_{mod}E_r^\infty, & \alpha \geq \alpha_{gel} \end{cases} \quad (2)$$

$$\nu_r = (1-\alpha)\nu_r^0 + \alpha\nu_r^\infty \quad (3)$$

Here, 0 and ∞ indicate the uncured and fully cured states, respectively, and the subscript r denotes the resin. The gel-point cure degree α_{gel} was set to 0.33, and the modified cure degree was defined as $\alpha_{mod} = \left(\alpha - \alpha_{gel}\right)/\left(1 - \alpha_{gel}\right)$.

The mechanical properties of the composite material can be calculated based on the properties of its constituent materials [25]. Since the rule of mixtures is considered fundamental knowledge within the composite materials field, the specific governing equations are omitted here for brevity.

Tables 2 and 3 summarize the material properties of T700s carbon fiber and H69 resin, respectively. The properties of T700s carbon fiber and H69 resin were obtained from the manufacturer's datasheets and relevant literature [27], while the chemical shrinkage coefficient was estimated from the volumetric shrinkage of the epoxy resin [28,29].

Table 2. Material properties of T700s carbon fiber.

Parameters	Values
Tensile moduli	$E_{f1} = 230$ GPa
	$E_{f2} = E_{f2} = 15$ GPa
Shear moduli	$G_{f12} = G_{f13} = 24$ GPa
	$G_{f23} = 5.03$ GPa
Tensile strength	$\sigma_A^+ = 4900$ MPa
Poisson's ratio	$v_{f12} = v_{f13} = 0.2$
	$v_{f23} = 0.398$
Coefficients of thermal expansion	$\beta_{f1} = -3.8 \times 10^{-7}\ K^{-1}$
	$\beta_{f2} = \beta_{f3} = 1.01 \times 10^{-5}\ K^{-1}$

Table 3. Material properties of H69 resin.

Parameters	Uncured Values	Cured Values
Tensile moduli	$E_r^0 = 33.39$ MPa	$E_r^\infty = 3013.20$ MPa
Shear moduli	$G_r^0 = 11.16$ MPa	$G_r^\infty = 1116$ MPa
Tensile strength	-	$\tau_A = 50$ MPa
Shear strength	-	$\tau_T = 30$ Mpa
Poisson's ratio	$v_r^0 = 0.4958$	$v_r^\infty = 0.35$
Coefficients of thermal expansion	$\beta_r^0 = 5.15 \times 10^{-5}$ K^{-1}	$\beta_r^\infty = 2.06 \times 10^{-5}$ K^{-1}
Coefficient of chemical shrinkage	$\beta_{chem} = 0.01$	

A linear elastic constitutive model was adopted to evaluate the stress evolution during curing [30].

$$\sigma_i(t) = \left[C_{ij}(t)\right]\varepsilon_j(t) \tag{4}$$

where $\sigma_i(t)$ and $\varepsilon_i(t)$ denote the stress and strain components at time t, respectively, and $\left[C_{ij}(t)\right]$ is the time-dependent stiffness matrix updated throughout the curing process. The non-mechanical strain consists of thermal strain and chemical shrinkage strain, which can be expressed as [31]:

$$\Delta\varepsilon_{\text{non-mechanical}} = \Delta\varepsilon_{\text{thermal}} - \Delta\varepsilon_{\text{chemical}} = \beta\Delta T - \beta_{chem}\Delta\alpha \tag{5}$$

where $\Delta\varepsilon_{\text{thermal}}$ and $\Delta\varepsilon_{\text{chemical}}$ denote the strain increments induced by thermal expansion and chemical shrinkage, respectively, while ΔT and $\Delta\alpha$ are the temperature increment and the increment in degree of cure.

2.1.2. Constitutive Behavior of CFRP

For the CFRP laminate, the elastic response was first described by the initial elastic constants. Once damage initiates, progressive failure was captured using the three-dimensional Hashin criterion [32], which accounts for four damage modes: fiber tension, fiber compression, matrix tension, and matrix compression. The corresponding damage variables were then used to degrade the stiffness matrix during the iterative analysis. As this formulation is well established, its detailed derivation is not repeated here.

2.1.3. Constitutive Behavior of Interface

The interlaminar delamination and SMA/matrix debonding were characterized using a bilinear cohesive zone model (CZM). Damage initiation was governed by the quadratic stress criterion, while the progressive softening and damage evolution were defined by a linear damage variable D based on the effective displacement δ_m. To account for the mixed-mode fracture behavior, the Benzeggagh–Kenane (B-K) criterion was employed to predict the critical energy release rate.

$$G^C = G_n^C + (G_s^C - G_n^C)\left\{\frac{G_s+G_t}{G_n+G_s+G_t}\right\}^\eta \tag{6}$$

This modeling approach effectively captures the transition from damage initiation to final debonding while maintaining computational efficiency for the complex U-shaped geometry. The CZM parameters employed in the numerical simulations are summarized in Table 4. These parameters were referenced from the works of Bogenfeld et al. [33] and Mohsin et al. [34].

Table 4. Material properties of CZM.

Parameters	Values	Parameters	Values
K_n	8000 MPa	t_t	62.5 MPa
K_s	12,000 MPa	G_n	0.5 mJ/mm^2
K_t	12,000 MPa	G_s	2.1 mJ/mm^2
t_n	25 MPa	G_t	2.1 mJ/mm^2
t_s	62.5 MPa		

2.1.4. Constitutive Behavior of SMA

The superelastic behavior of the SMA was described by a constitutive framework incorporating the stress–strain relation, martensitic volume fraction evolution, and the corresponding transformation loading criterion. This formulation enables an accurate representation of the phase transformation and hysteretic response of NiTi alloys under finite deformation. In the present study, the constitutive equation was expressed in an Eulerian rate form.

$$\overset{\circ}{\tau} = 2\mu\overline{\boldsymbol{D}^e} + \mathrm{K}\dot{\delta}\mathbf{1} \tag{7}$$

Here, $\overset{\circ}{\tau} = \dot{\boldsymbol{\tau}} - \boldsymbol{W\tau} + \boldsymbol{\tau W}$ denotes the Jaumann rate of the Kirchhoff stress τ; μ and K are the shear and bulk moduli, determined by Young's modulus E and Poisson's ratio ν. $\overline{D^e}$ represents the deviatoric elastic stretching tensor, $\dot{\delta}$ is the volumetric deformation rate, $\mathbf{1}$ is the second-order identity tensor.

The phase transformation from austenite to martensite is treated as a first-order diffusionless solid-state transition. Its evolution is described by the martensite volume fraction $\phi(0 \le \phi \le 1)$, governed by

$$\dot{\phi} = \gamma\mathcal{S}(A_\phi) \tag{8}$$

where γ represents the non-negative transformation multiplier, $\mathcal{S}(\cdot)$ is the sign function, and A_Φ denotes the transformation driving force, expressed as

$$A_\phi = \mathcal{H}\left(\overline{M_e} : n_t - \phi\mathcal{H}\mu^t - \iota^t\right) - \Delta_\eta(\theta - \theta_0) - z^t - \iota^\phi \tag{9}$$

where $\mathcal{H}$ denotes the saturation transformation strain, $\overline{M_e}$ is the symmetric traceless Mandel stress, and n_t defines the transformation strain direction. μ^t is the transformation hardening modulus; ι^t and ι^ϕ are the non-negative Lagrange multipliers enforcing the physical con-

straints. Δ_η represents the entropy difference between austenite and martensite, θ and θ_0 are the current and reference temperatures, and z^t controls the nonlinear phase transformation.

The loading function specifies the onset condition for phase transformation under general loading paths. In the present formulation, it is defined in terms of the driving force as

$$F_\phi = \left|A_\phi\right| - Y(\phi) \tag{10}$$

where Y is the transformation threshold related to the martensite volume fraction, and its detailed expression is given in the authors' previous study [35]. When internal hysteresis is neglected, it degenerates into a constant Y_0. The loading function thus governs the onset and progression of martensitic transformation.

2.2. Experiment Setup

2.2.1. Material Properties of SMA

Uniaxial tensile tests were performed on a Test Resources 100 kN testing machine manufactured by Sens Testing Instrument Co., Ltd. (Shenzhen, China) to obtain the stress–strain behavior of the SMA wire. Each specimen had an effective gauge length of 100 mm and was tested at a loading rate of 3 mm/min. Five repeated tests were carried out under identical conditions, and the median response curve was selected for Figure 1a.

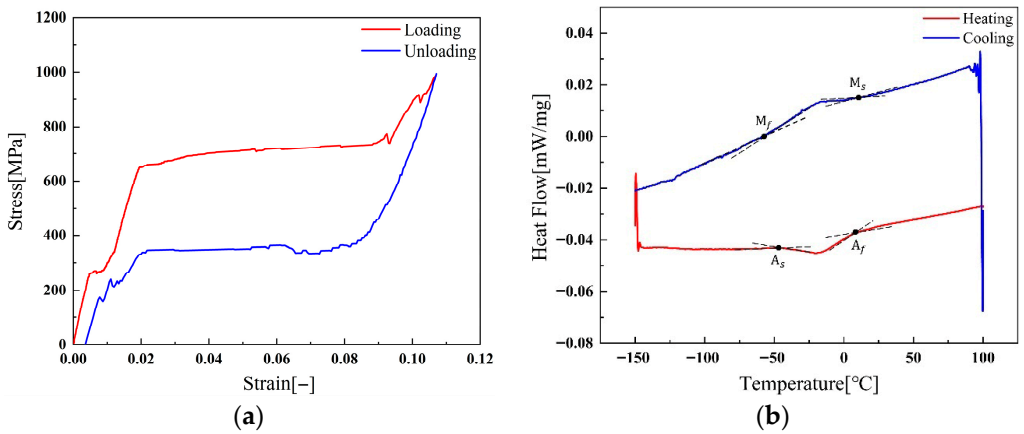


Figure 1. Material testing of SMA wire: (**a**) stress–strain curve and (**b**) DSC curve.

During the loading–unloading cycles, the SMA wire exhibits two distinct characteristics: significant superelastic deformation and a dissipative hysteresis loop. It should be noted that the small oscillations observed in the unloading branch of Figure 1a were not explicitly reproduced in the numerical model. The constitutive parameters of the SMA were identified from the average response of five repeated tensile tests, and the simulation was intended to capture the mean superelastic behavior, including the loading/unloading stiffness, transformation plateau stress, hysteresis width, and residual strain, rather than pointwise fluctuations in the experimental signal. Since the constitutive model does not include stochastic measurement noise or localized transformation-front serration, these small-amplitude oscillations were not introduced into the numerical response. During unloading, the stress-induced martensite transforms gradually back into austenite, and the localized evolution of the transformation front may produce small stress serrations or plateau undulations.

In addition, the small residual strain remaining after unloading is a typical characteristic of superelastic shape memory alloys, arising from transformation-induced plasticity during the phase transformation process.

The maximum recoverable strain exceeds 6.5%, with a phase transformation stress from austenite to martensite approximately at 700 MPa, and an elastic modulus of 58.5 GPa for austenite, 33.3 GPa for martensite.

Three DSC tests were performed on the superelastic SMA wires, and the average results are shown in Figure 1b. The superelastic SMA employed in this work exhibits transformation temperatures of $A_s = -46.7\ ^\circ C$, $A_f = 7.4\ ^\circ C$, $M_s = 8.4\ ^\circ C$, and $M_f = -60.6\ ^\circ C$, ensuring that the material remains fully austenitic at room temperature.

2.2.2. Manufacture of Laminate

U-shaped leading-edge specimens were fabricated using an autoclave process with T700/H69 carbon/epoxy prepregs with a nominal ply thickness of 0.125 mm. A pure CFRP control group and an SMA-reinforced CFRP group were prepared for comparative analysis. Both configurations featured a 20-ply layup, resulting in a total thickness of 2.5 mm. The stacking sequence for the CFRP was $[0_2/90_2/0_2/90_2/0_2/0_2/90_2/0_2/90_2/0_2]$ while the SMA-CFRP followed a $[0_2/90_2/0_2/90_2/0_2/0_2/90_2/0_2/W/90_2/0_2]$ sequence, where 'W' denotes the SMA wire.

The reinforcement consisted of superelastic NiTi wires with a diameter of 0.3 mm. Precise spatial distribution was achieved using a custom 3D-printed PLA alignment frame, which ensured a consistent wire pitch of 6 mm through a perforated edge-fixation system.

A custom-designed split-die mold was employed to fabricate the U-shaped leading-edge components. This two-part configuration ensures uniform load distribution and dimensional precision throughout the consolidation cycle. Constructed from high-strength, corrosion-resistant stainless steel, the tooling is engineered to sustain the rigorous thermal and baric conditions of the autoclave process. The symmetric U-shaped geometry of the die and punch (top and bottom molds) was optimized to facilitate both resin rheology during infusion and efficient post-cure demolding. To ensure accurate spatial positioning and consistent pretension, the SMA wire grid was integrated into the designated prepregs with high precision, as illustrated in Figure 2a.

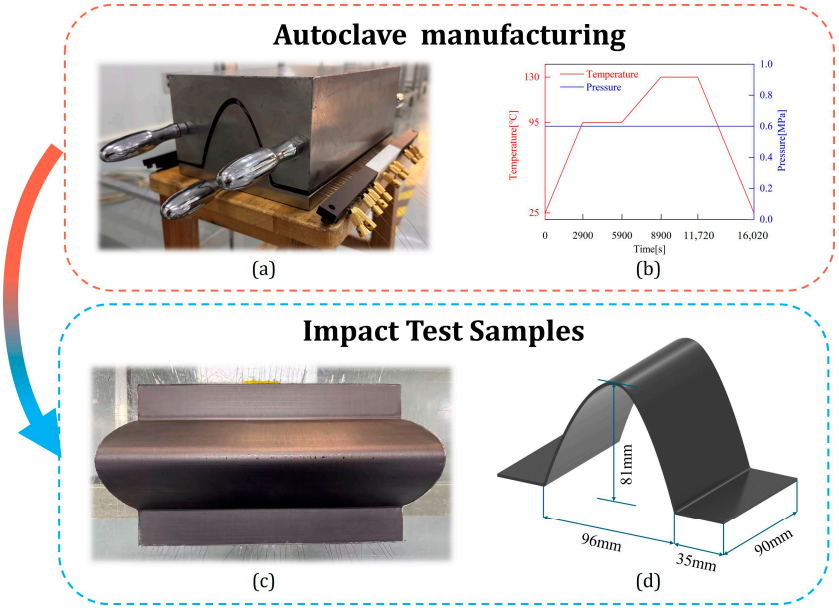


Figure 2. Specimen preparation process: (**a**) SMA-CFRP laid up in the mold; (**b**) curing cycle; (**c**) fabricated U-shaped specimen; and (**d**) geometric dimensions of the impact specimen.

Upon completion of the layup, the specimens were cured in an autoclave following the process cycle illustrated in Figure 2b. The cycle commenced with a heating ramp of

1.46 °C/min from room temperature to a 95 °C dwell for 50 min, promoting resin rheology and consistent impregnation. The temperature was then elevated at 0.7 °C/min to 130 °C and held for 47 min to ensure full cross-linking. A controlled cooling phase to ambient temperature followed, aimed at mitigating thermal-stress-induced microstructural defects.

The cured specimens are shown in Figure 2c. Following the consolidation process, the surface flatness and edge profiles were initially inspected. High-pressure water-jet machining was then utilized to rectify the edge profiles and remove excess flash, ensuring geometric regularity and eliminating potential boundary-effect errors during testing. Following edge refinement, specimen warpage was precisely characterized via a non-contact optical measurement system. The components were finally precision-cut to the standardized dimensions required for low-velocity impact testing, as depicted in Figure 2d, ensuring full compliance with testing protocols.

2.2.3. Low-Velocity Impact

The specimens used in this experiment are complex-shaped components. To ensure precise positioning and stability during testing, a combination of a custom aluminum alloy frame and traditional fixtures was employed to securely fix the specimen beneath the impactor. This clamping method effectively prevented any displacement or unwanted deformation of the specimen during the impact process. Low-velocity impact tests were conducted on a WANCE DIT203Z1 testing machine manufactured by Wance Testing Equipment Co., Ltd. (Shenzhen, China). The impact assembly, consisting of the hammer body and a hemispherical impactor, had a total mass of 20.99 kg and an impactor diameter of 16 mm. To achieve the target impact energy of 40 J, the initial velocity was set to 1.95 m/s. Additionally, an anti-rebound device at the base of the machine effectively caught the impactor after the initial strike, preventing secondary impacts and ensuring the accuracy of the data and the integrity of the specimen. Three replicate tests were conducted for each specimen, and the median curve was selected for comparative analysis. The experimental setup is shown in Figure 3.

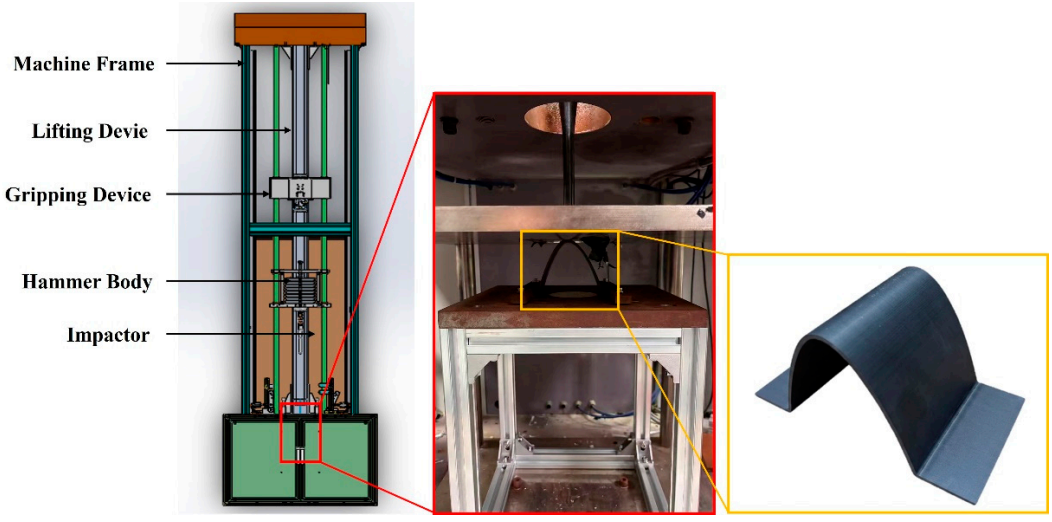


Figure 3. Low-velocity impact equipment.

Figure 4 illustrates the mechanical responses of CFRP and SMA-CFRP under impact, presenting both the raw data and the curves automatically smoothed by the testing machine. Post-smoothing, the initial force values for both materials do not originate from zero. This phenomenon is attributed to the baseline offset of the piezoelectric force sensors and the integrated signal filtering procedures of the impact testing system. Such offsets do not affect

the peak force or the overall impact response. For consistency in comparative analysis, the automatically smoothed curves are adopted for all subsequent investigations.

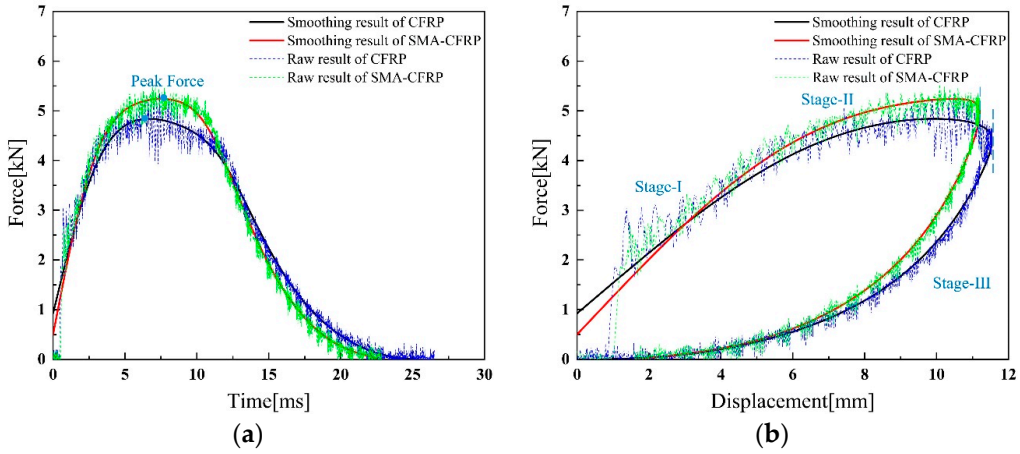


Figure 4. Comparison of experiment results between CFRP and SMA-CFRP: (**a**) the force–time curve; and (**b**) force–displacement curve.

In addition, interfacial phenomena such as slip and debonding may occur between the SMA wires and the surrounding matrix during impact. However, the influence of these complex interfacial effects on curve fluctuations is difficult to quantify in a rigorous manner. Therefore, the present study focuses on the smoothed force-response curves for analysis, and these curves are further used to validate the accuracy of the subsequent numerical simulations.

The force–time curves for the two materials are shown in Figure 4a. At the onset of impact, both materials exhibited elastic behavior, with the impact force rising rapidly. The pure CFRP U-shaped leading edge reached a peak force of 4831.76 N at approximately 6.2 ms, whereas the SMA-CFRP counterpart reached 5239.42 N at 7.4 ms, representing an 8.44% increase. This result indicates that the integration of SMA wires significantly enhances the impact resistance of the U-shaped leading edge, enabling it to withstand higher transient impact loads.

The low-velocity impact force–displacement curves of the U-shaped leading edge can be divided into three stages, corresponding to distinct mechanical response processes: the elastic stage, the damage evolution stage, and the unloading stage, as shown in Figure 4b. Analyzing stage I reveals that the stiffness of SMA-CFRP is slightly higher than that of CFRP, with an increase of approximately 4.66%. This marginal improvement indicates that the introduction of SMA wires enhances the material rigidity, providing higher resistance to deformation. In stage II, the maximum displacement of the impactor was 11.54 mm for the CFRP leading edge and 11.20 mm for the SMA-CFRP version. Although the displacement difference is small, it stems primarily from structural flexibility. The relatively larger deformation in CFRP leads to pronounced bending strains, resulting in compressive failure on the impacted surface and tensile failure on the back surface. Conversely, the smaller displacement in SMA-CFRP reflects increased rigidity, which concentrates the impact load and yields a higher peak force.

Typical low-velocity impact energy absorption curves can be characterized by two primary values: the impact energy, representing the total energy applied to the specimen, and the absorbed energy, representing the energy dissipated by the specimen, as shown in Figure 5. Energy dissipation begins when the impactor contacts the specimen, and the impact energy is transferred through elastic bending and various damage mechanisms. The peak inflection point of the energy curve occurs when the impactor's velocity drops to zero. Subsequently, the elastic strain energy stored in the specimen is returned to

the impactor until separation, at which point the energy curve rapidly descends to a stabilized value.

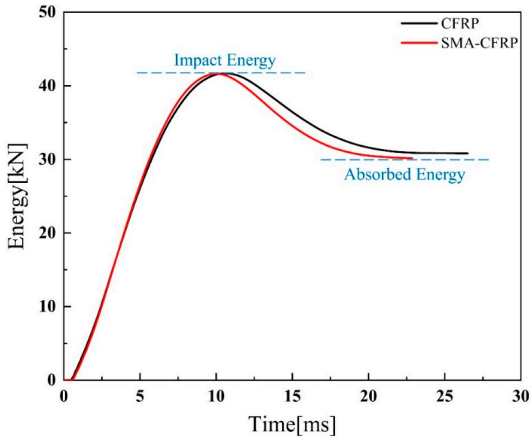


Figure 5. Comparison of energy–time curves between CFRP and SMA-CFRP.

The energy absorbed by the CFRP leading edge can be regarded as the total energy dissipated during internal damage. This energy primarily stems from damage processes such as crack propagation, matrix failure, and interlaminar delamination. In low-velocity impacts, the energy consumed by fiber breakage is minimal and can be neglected. For the SMA-CFRP leading edge, the energy absorption process includes not only composite damage but also the energy dissipated by the pseudoelastic SMA wires through phase transformations during loading-unloading cycles and wire pull-out from the matrix.

Observing the peak impact energy reveals a hysteresis phenomenon in the response of the CFRP specimens. This hysteresis is closely related to the gradual accumulation of damage. As damage intensifies, the integrated transverse stiffness of the laminate decreases, reducing the impactor's acceleration and extending the energy release duration. When damage becomes more severe, the timing of the peak energy is delayed accordingly. This phenomenon indicates that the mechanical response of CFRP degrades under impact, ultimately affecting energy absorption efficiency and damage evolution.

Accordingly, the energy dissipation within the CFRP U-shaped leading edge is formulated as follows:

$$E^C_{Absorbed} = E^C_{mc} + E^C_{de} \tag{11}$$

Conversely, the total energy dissipation within the SMA-CFRP U-shaped architecture is formulated as follows:

$$E^S_{Absorbed} = E^S_{mc} + E^S_{de} + E^S_{sma} \tag{12}$$

where E_{mc} is energy dissipated by matrix cracking, E_{de} is energy dissipated by delamination. The superscripts C and S represent the two types of specimens, respectively. E_{sma} denotes the energy dissipation associated with the stress-induced phase transformation of the superelastic SMA wires and their interfacial pull-out from the resin matrix.

Combining the previous analysis of mechanical response with the energy absorption data for the two U-shaped architectures, it is observed that the pure CFRP leading edge underwent greater structural deformation during impact due to its lower flexural stiffness, thus forcing it to absorb more impact energy. In sharp contrast, the SMA-CFRP structure, reinforced by the embedded SMA wires, demonstrated higher structural impedance and energy modulation capabilities. Consequently, its total energy absorption remained lower than that of the pure CFRP, satisfying the relationship $E^C_{Absorbed} > E^S_{Absorbed}$.

The discrepancy in energy dissipation is further elucidated by the damage-related inequality $E^C_{mc} + E^C_{de} > E^S_{mc} + E^S_{de}$, which implies that the baseline CFRP structure un-

derwent more extensive matrix cracking and delamination. Conversely, the integration of SMA wires effectively inhibited the progression of irreversible structural degradation. By absorbing energy through reversible phase transformations, the SMA reinforcement significantly augments the overall damage tolerance of the U-shaped leading edge.

2.3. Finite Element Simulations

To investigate the influence of the curing process on the low-velocity impact resistance of the U-shaped structure, a thermo-chemo-mechanical coupled curing simulation was first performed for both configurations to extract their residual stress distributions. Subsequently, these residual stresses were incorporated into the low-velocity impact model as a predefined initial field. By comparatively analyzing the impact load response, damage evolution morphology, and experimental data, the impact resistance mechanisms of SMA-reinforced CFRP were thoroughly revealed, accounting for the initial stress state.

2.3.1. Curing Simulation Models

The curing finite element model established in this study maintains high geometric fidelity with experimental specimens. The model is discretized into 10 layers of solid elements along the thick direction, treating plies with the same orientation as an anisotropic continuum by assigning material orientations. Regarding the integration of SMA wires, the model strictly follows the experimental layup paths. Based on curing kinetic equations, a dynamic constitutive characterization accounting for chemical shrinkage and thermal stress was implemented via the ABAQUS user subroutine UMAT.

A gradient meshing strategy using C3D8 elements was implemented to optimize computational fidelity and efficiency. A 3.0 mm global mesh was utilized, whereas the impact-sensitive region featured a refined 1.0 mm mesh to capture high-gradient load transfer accurately. Boundary conditions involved an encastred upper surface during the curing cycle, which was subsequently released to simulate demolding-induced spring-back. The autoclave environment was replicated by applying thermal and baric loads along predefined temporal paths. The numerical framework was ultimately benchmarked against experimental results, showing excellent agreement in the curing deformation profiles of both the CFRP and SMA-CFRP specimens.

2.3.2. Low-Velocity Impact Models Incorporating Residual Stress

The simulation framework is presented in Figure 6. To incorporate curing-induced residual stresses into the impact model, a curing simulation model with identical dimensions to the low-velocity impact (LVI) model was developed. SMA wires were embedded into the CFRP matrix using the 'embedded region' interaction, with the spacing between wires consistent with the experimental setup. To replicate the experimental clamping conditions, the two flanges of the U-shaped leading edge were fully constrained. The impactor was modeled as a rigid body with a predefined initial velocity field of 1.95 m/s and a mass of 21 kg, matching the experimental parameters. The mesh size and element attributes of the LVI model remained consistent with the curing model. To prevent premature termination of the simulation due to severe element distortion caused by stiffness degradation, an element deletion mechanism was introduced in the user subroutine, effectively enhancing the stability and convergence of the model.

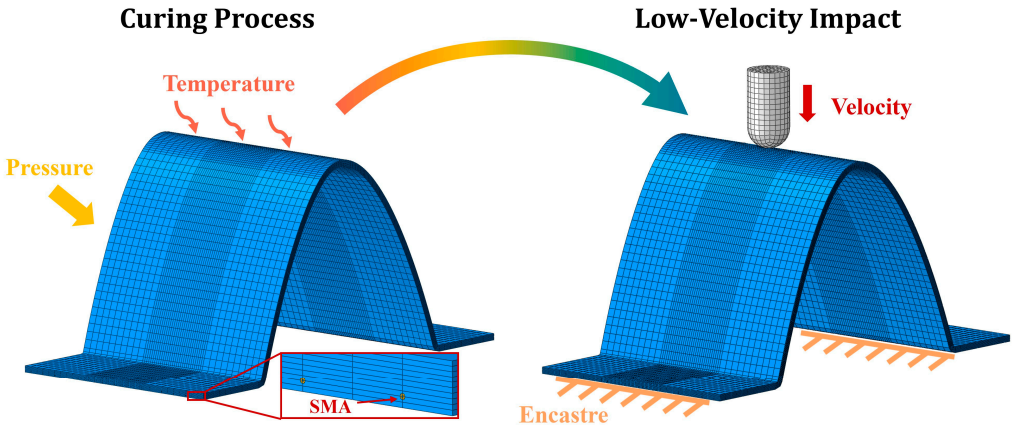


Figure 6. Computation framework of the curing process and LVI resistance of U-shaped CFRP.

3. Results and Discussion

This chapter systematically characterizes the curing deformation behavior and evaluates the LVI resistance performance of CFRP and SMA-CFRP U-shaped structures, accounting for residual stress effects. By integrating experimental testing with numerical simulations, the influence of curing-induced residual stresses on the structural mechanical response is thoroughly investigated. Furthermore, the stress transfer paths and reinforcement strategies of SMA-CFRP under dynamic loading are elucidated, providing a theoretical foundation for the impact-resistant design of high-performance leading-edge structures.

3.1. Curing Deformation

Figure 7 illustrates the evolution of the degree of cure for the thermosetting resin throughout the curing process. As shown, during the initial preheating stage, the reaction kinetics are weak due to the relatively low temperature, resulting in a slow curing reaction and a minor increase in the degree of cure. As the temperature enters the second heating ramp, the autocatalytic reaction mechanism becomes prominent, causing the reaction rate to rise sharply and the curing process to accelerate significantly; consequently, the degree of cure exhibits a rapid growth trend. During the subsequent dwell stage, the temperature is maintained at a high and constant level, facilitating the continued reaction. Although the reaction rate gradually slows down, the degree of cure continues to increase steadily, ultimately reaching approximately 0.96, indicating that the resin is substantially cured.

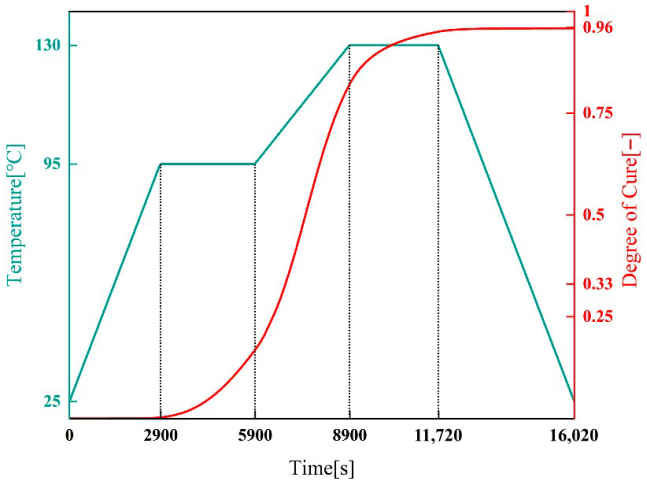


Figure 7. Temperature and cure degree curves of CFRP.

To measure experimental curing deformation, a non-contact image acquisition method was utilized to determine the relative position between the warped flange and the mold edge. By extracting pixel data and applying a scale factor, the pixel differences were converted into physical length units. In the finite element simulation, the displacement distribution of the laminate in the thickness direction was output upon completion of the curing process. Finally, the Z-direction deformation data from the free-edge nodes of the simulation model were extracted and compared with the experimentally measured warpage for verification. As shown in Figure 8.

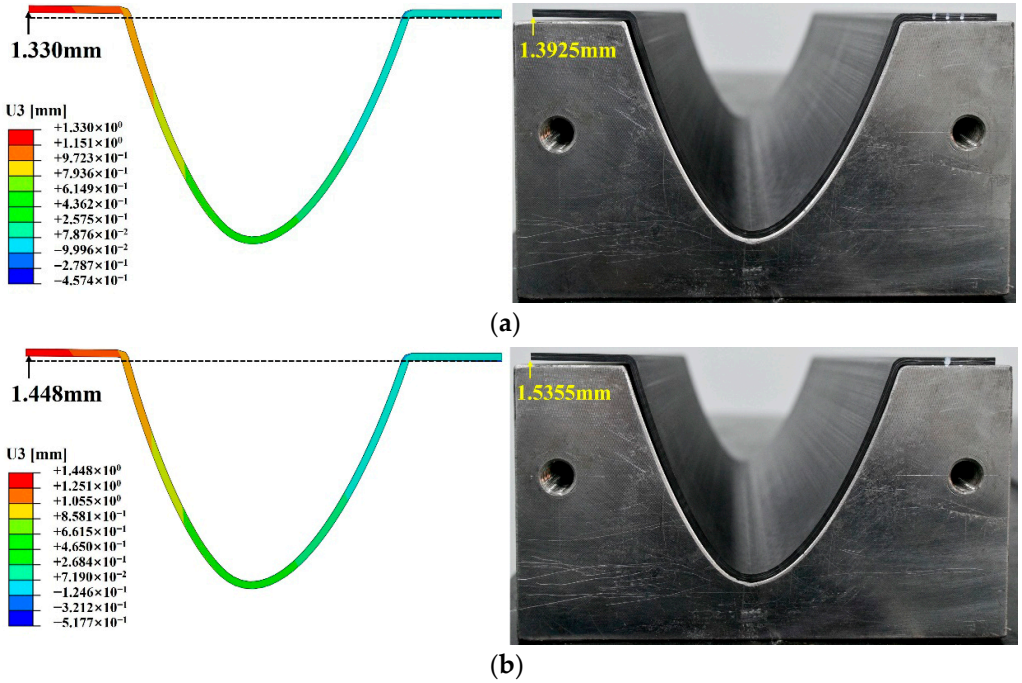


Figure 8. Comparison between simulated curing deformation and experimental warpage. (**a**) CFRP and (**b**) SMA-CFRP.

To verify the accuracy of the numerical curing model, this study compared the curing-induced warpage of pure CFRP and SMA-CFRP U-shaped structures. For the pure CFRP structure, the experimental maximum warpage was 1.39 mm, while the simulation predicted 1.33 mm, resulting in a relative error of 4.32%. For the SMA-CFRP structure, the experimental and simulated values were 1.54 mm and 1.45 mm, respectively, with the error maintained at 5.84%. These comparative results demonstrate that the multi-field coupled curing model developed in this study can capture the physical evolution of the composite during the molding process with high precision, fully validating the model's effectiveness in predicting curing deformation and residual stress distribution.

3.2. Curing-Induced Residual Stress

Building upon the validated fidelity of the curing simulation for both CFRP and SMA-CFRP U-shaped architectures, the three-dimensional residual stress fields at the end of the curing cycle were quantified and analyzed. These results serve as the predefined initial stress field for the subsequent coupled analysis of the residual stress effects during the dynamic loading (or impact) event. This integrated modeling approach ensures the continuity of the thermo-mechanical history from manufacturing to structural response.

As the composite laminate is modeled with local material coordinate systems and direction-dependent mechanical properties, the entire system exhibits typical anisotropic behavior. For this reason, conventional isotropic metrics such as von Mises equivalent

stress are insufficient for capturing the internal stress state. Instead, the longitudinal stress component (S11) along the fiber orientation was utilized as the primary metric for residual stress characterization. S11 directly reflects the tensile and compressive states in the principal fiber direction, offering greater physical significance for understanding interfacial debonding, fiber failure, and structural deformation trends.

Simulation results indicate that the pure CFRP U-shaped leading edge exhibits significant residual stress characteristics after demolding. As shown in Figure 9a, the maximum residual stress in the S_{11} direction reaches -59.63 MPa. As indicated by the red circle in Figure 9a, the residual stress displays a pronounced spatial heterogeneity, with high-stress concentrations primarily localized in the transition region between the U-shaped curved section and the flat flange sections. This phenomenon is attributed to the stress concentration effect caused by the geometric transition: during the curing shrinkage process, the constrained anisotropic contraction at the curved region leads to a complex stress gradient.

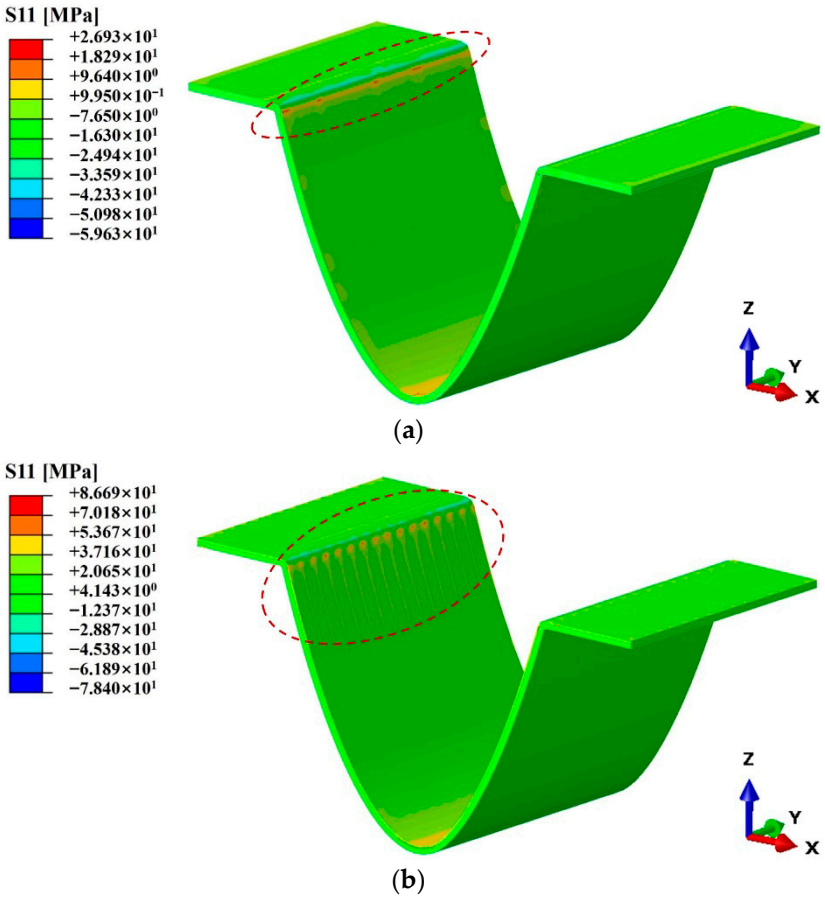


Figure 9. Residual stress field predicted by curing simulation. (**a**) CFRP and (**b**) SMA-CFRP.

As observed from the stress contours, the main body of the U-shaped leading edge is generally under a state of compressive stress. However, in the critical transition regions, the stress state undergoes a sharp transformation, characterized by the coexistence of both compressive and tensile stresses. Specifically, large tensile stresses tend to accumulate at the inner radius of the transition zone, while compressive stresses appear at the outer radius. This in-plane stress coupling is the core mechanical factor leading to the structural warpage.

To more intuitively reveal the influence of the reinforcement phase on the matrix stress field, Figure 9b shows the S11 stress distribution in the CFRP matrix with the SMA wires hidden. Comparing it with the pure CFRP leading edge, it can be observed that the introduction of SMA wires significantly alters the initial stress state of the matrix.

Simulation results show that significant band-like stress concentrations appear in the regions where SMA wires are embedded. More importantly, this local stress induced by the reinforcement phase undergoes strong linear superposition and coupling with the geometric stress concentration in the U-shaped transition zone, as shown by the red circle in Figure 9b. This coupling effect causes the maximum residual stress in the transition zone to surge to +86.69 MPa.

The fundamental mechanism driving this stress escalation is the pronounced Coefficient of Thermal Expansion mismatch between the SMA reinforcements and the CFRP. During the cool-down stage of the curing cycle, the differential shrinkage between the SMA wires and the resin matrix precipitates a severe interfacial thermo-mechanical incompatibility. As the SMA wires exert localized macroscopic constraints on the matrix, this reinforcement-induced restraint is significantly magnified within the transition zones characterized by geometric discontinuities. This synergy culminates in a highly complex stress concentration regime.

To reveal the detailed stress state of the SMA, Figure 10 illustrates the von Mises stress contour of the SMA wire after curing. It can be observed that stress exhibits a non-uniform distribution along the wire, with high-stress regions significantly concentrated at the bent locations. Specifically, the peak stress occurs in the geometric transition zone corresponding to the U-shaped structure clamping edge, reaching a maximum value of 267.7 MPa, as shown by the red circle in Figure 10. This indicates that this region underwent the most intense strain gradients during the curing process. In contrast, the SMA wire in the straight sections maintains a lower and more stable stress level, ranging from 142.8 MPa to 178.5 MPa. This spatial heterogeneity in stress is primarily attributed to the geometric constraints and local compression exerted by the U-shaped structure.

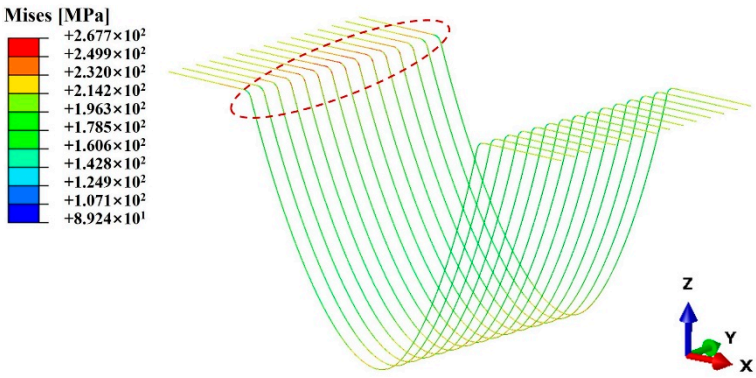


Figure 10. Curing-induced residual stress in SMA wires.

The essence of the high compressive stresses in the SMA wires lies in the thermodynamic property differences between the wires and the CFRP matrix. During the autoclave cooling stage, the shrinkage of the CFRP matrix is much greater than that of the SMA wires, causing the matrix to exert inward compressive forces on the wires through interfacial shear. In the transition zones of the structural corners, the stress concentration effect caused by the geometric curvature overlaps with the matrix shrinkage, creating extremely high three-dimensional constraint pressures and making these locations peak stress regions.

3.3. Effect of Residual Stress on Low-Velocity Impact Response

This section provides a systematic and in-depth analysis of the results obtained from the LVI finite element simulations, with comparisons made against the experimental data to verify the accuracy and reliability of the numerical model. The damage trends of the two materials are qualitatively analyzed by comparing the backside morphologies of the U-shaped specimen post-impact. Furthermore, the influence of curing residual stresses on

the impact resistance of both specimens is quantitatively evaluated through a comparative analysis of the force–time, force–displacement, and energy–time curves.

3.3.1. CFRP U-Shaped Leading Edge

Figure 11 illustrates the post-impact damage morphologies on the back face of the CFRP U-shaped leading edge, providing a comparative assessment between experimental observations and numerical predictions. As depicted in Figure 11a, the backside of the specimen primarily sustains tensile loading during the impact event, resulting in significant fiber breakage, as highlighted by the red dashed circles. Concurrently, matrix cracking initiates and propagates around the impact zone, developing into a discernible fracture network, as indicated by the yellow dashed circles.

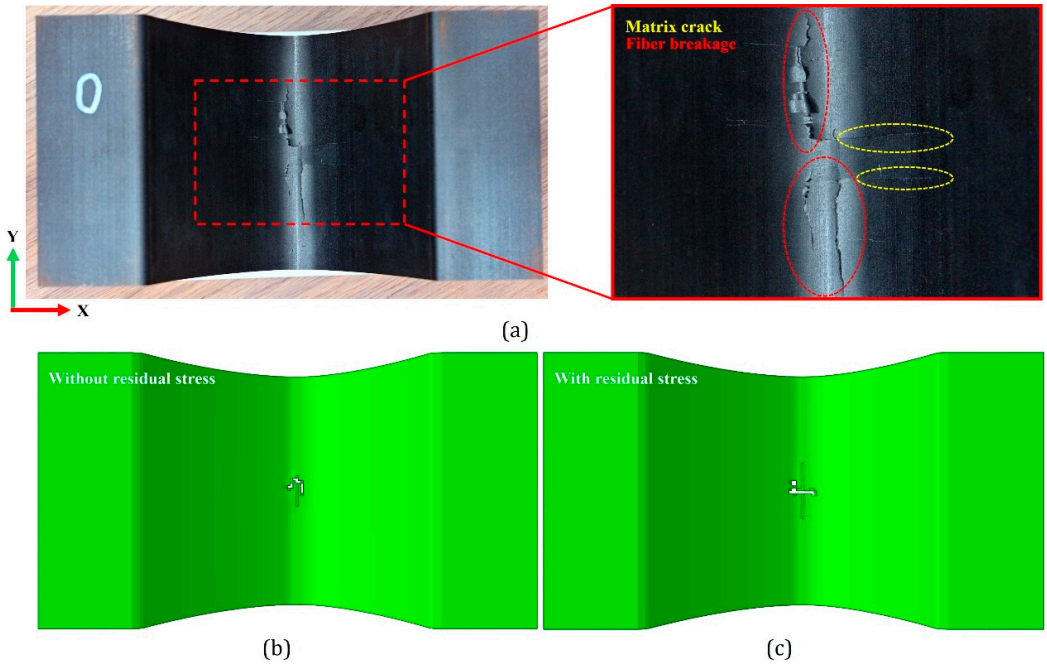


Figure 11. Comparison between experimental photographs and simulation results: post-impact backside damage of CFRP U-shaped structure: (**a**) experiment result; (**b**) simulation result without residual stress; and (**c**) simulation result with residual stress.

Figure 11b presents the simulation results without incorporating curing-induced residual stresses, where the visible voids correspond to element deletion due to failure. While this model captures the fundamental failure modes, the predicted damage area and crack lengths are significantly underestimated compared to the experimental evidence. In stark contrast, Figure 11c illustrates the numerical results after accounting for the curing residual stress. The introduction of internal stress notably exacerbates the crack evolution process, yielding a damage morphology that exhibits higher fidelity to the experimental results. This enhanced correlation demonstrates that residual stress effectively lowers the threshold for damage initiation and promotes crack propagation. Furthermore, it underscores the necessity of considering curing-induced effects to achieve accurate predictions of low-velocity impact performance.

Figure 12 presents the comparative results of the force–time and force–displacement curves for the CFRP U-shaped leading edge under low-velocity impact. By comparing the two numerical simulations with the experimental data, it is evident that the model incorporating residual stress offers significant advantages in both predictive accuracy and the characterization of mechanical behavior evolution.

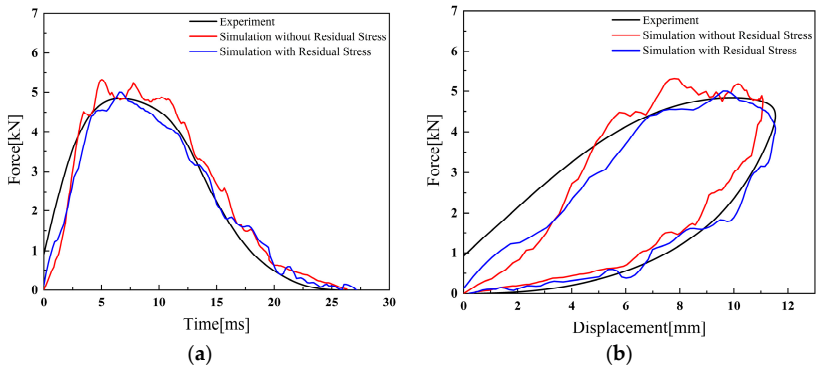


Figure 12. Comparison between experiment and simulation response of CFRP during the impact process: (**a**) the force–time curve; and (**b**) force–displacement curve.

Regarding the peak load, the simulation neglecting curing-induced residual stresses yields a predicted value of 5.29 kN, which is approximately 9.3% higher than the experimental value of 4.84 kN, representing a clear overestimation. Upon the inclusion of curing residual stress, the predicted peak force decreases to 5.01 kN, significantly reducing the relative error to 3.5%. This demonstrates that the initial internal stresses generated during the curing process weaken the instantaneous load-bearing capacity of the structure. Furthermore, this pre-loading effect causes the material to enter the damage evolution stage prematurely.

In addition, the force–displacement curves reflect the stiffness characteristics of the material during the impact process. Observations indicate that the simulation incorporating residual stresses aligns more closely with the experimental curves in terms of both the structural dynamic stiffness in the loading phase and the trajectory of the unloading phase compared to the model neglecting residual stresses. In the absence of residual stress, the curves exhibit more violent fluctuations and higher peak values, suggesting that the model is overly stiff. Conversely, the introduction of residual stress exerts a softening effect, enabling the numerical model to more realistically simulate the stiffness degradation process induced by matrix cracking and delamination.

Figure 13 presents the comparison of energy–time curves for the CFRP U-shaped leading edge under low-velocity impact. By comparing the experimental data with the two numerical simulation results, the significant influence of curing-induced residual stresses on the energy absorption characteristics of the structure is clearly observable. Regarding the overall trend of the curves, the total impact energy in all three cases remains at approximately 40 J, indicating consistency in the external loading conditions. However, distinct differences emerge among the three curves during the energy unloading phase.

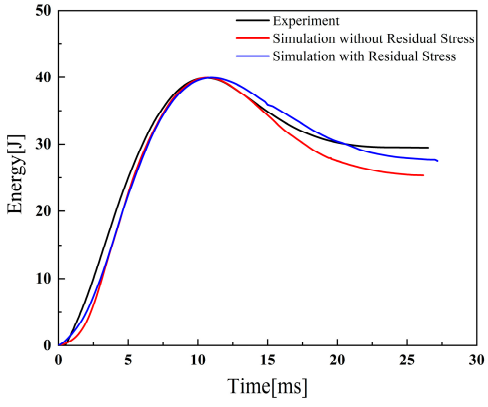


Figure 13. Comparison between experiment and simulation response: the energy–time curve of CFRP during the impact process.

The model neglecting residual stresses exhibits the lowest final absorbed energy. This indicates that the model possesses excessive structural rigidity and sustains less internal damage during the impact, thereby returning a greater portion of the deformation energy to the impactor in the form of elastic recovery. This overestimation of stiffness leads to a deviation in the predicted energy absorption values. In contrast, the model incorporating residual stresses shows a significant increase in final absorbed energy, with an evolution trajectory that closely matches the experimental curve. This is attributed to the fact that the introduction of curing residual stresses places the structure in a pre-stressed state, effectively lowering the critical threshold for damage initiation. Consequently, this model generates more extensive matrix cracking and delamination failure during the impact, dissipating a larger amount of energy through irreversible damage evolution.

The experimentally measured final absorbed energy is 29.5 J. The simulation model neglecting residual stresses yields a steady-state value of 25.3 J, resulting in a relative error of 16.6% compared to the experimental data. In contrast, upon the incorporation of residual stress, the absorbed energy reaches 27.7 J, reducing the relative error to 6.5%. This improved correlation more accurately reflects the energy balance process of the actual structure under impact loading.

3.3.2. SMA-CFRP U-Shaped Leading Edge

Figure 14 illustrates the post-impact damage on the backside of the SMA-CFRP U-shaped leading edge, providing a comparative validation between experimental observations and numerical simulations. First, the experimental results in Figure 14a indicate that the back face sustains severe tensile loading at the moment of impact, leading to the fiber breakage highlighted by the red dashed circles. However, the overall degree of damage is significantly lower than that observed in pure CFRP specimens. This indicates that the embedded superelastic SMA wires provide an effective reinforcing effect, suppressing crack propagation into deeper layers by absorbing strain energy. Concurrently, the matrix cracking indicated by the yellow dashed circles manifests as finer and more localized cracks, suggesting that the interfacial shear effect between the SMA wires and the resin matrix partially redistributes the failure load.

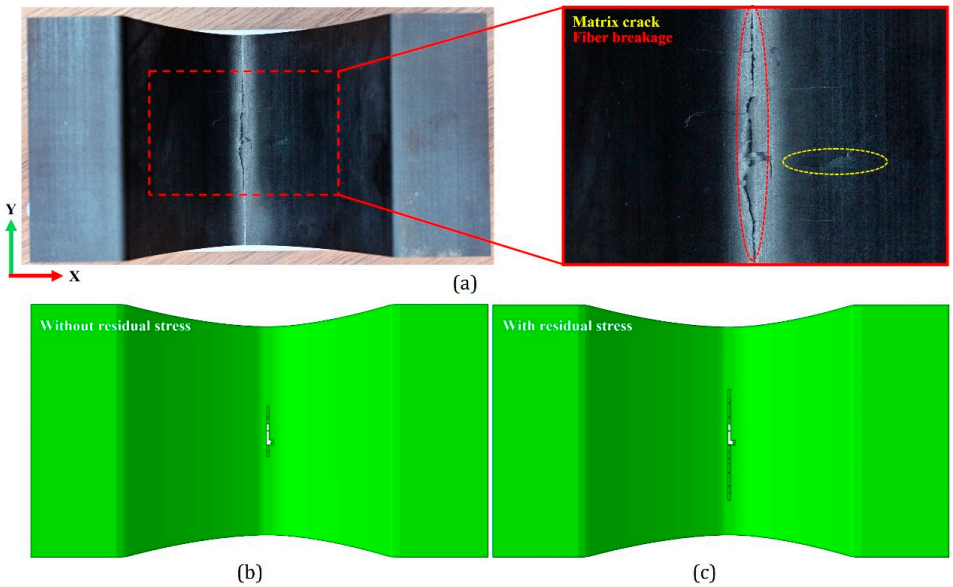


Figure 14. Comparison between experimental photographs and simulation results: Post-Impact backside damage of SMA-CFRP U-shaped Structure: (**a**) experiment result; (**b**) simulation result without residual stress; and (**c**) simulation result with residual stress.

Figure 14b,c presents the simulation results obtained with and without the consideration of curing-induced residual stresses, respectively. A comparative analysis reveals that the model neglecting these residual stresses predicts impact crack lengths that are significantly shorter than the experimental observations, with the damage area appearing overly localized. This discrepancy suggests that ignoring the initial internal stresses leads to an overestimation of structural rigidity in the numerical model, rendering it unable to accurately capture the damage initiation during the early stages of impact.

In contrast, the model incorporating the residual stress field yields crack evolution trajectories and lengths that are in high agreement with the experimental results. The presence of residual stress brings the material closer to its failure threshold, thereby providing a more realistic representation of the damage propagation laws driven by the superposition of complex stresses under impact loading.

To facilitate the understanding of the superelastic deformation and martensitic phase transformation of the SMA wires during the impact, Figure 15 displays the deformation and martensitic volume fraction contours of the SMA wires at the moment of maximum deflection. Under the intense impact force, the entire SMA mesh structure undergoes significant concave deformation in the central region. The red regions along the wires indicate where the austenite has completely transformed into martensite. Upon rebounding, the SMA mesh fully recovers to its original configuration. This entire loading and unloading process involves substantial energy dissipation, which effectively mitigates the risk of damage to the composite matrix.

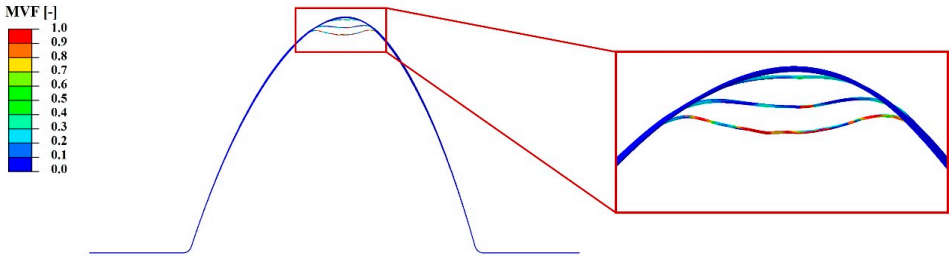


Figure 15. The martensite volume fraction of SMA wires at the moment of maximum deflection.

Figure 16 presents a comparison of the force–time and force–displacement curves for the SMA-CFRP U-shaped leading edge under low-velocity impact. The accuracy of the model in simulating complex material systems is further validated through a fitting analysis that compares numerical simulations—both with and without the inclusion of curing-induced residual stresses—against experimental data.

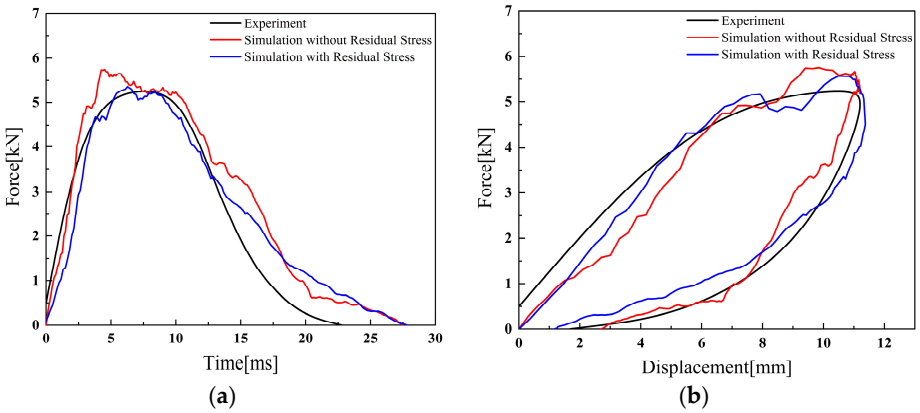


Figure 16. Comparison between experiment and simulation response of SMA-CFRP during the impact process: (**a**) the force–time curve; and (**b**) force–displacement curve.

Regarding the load-bearing characteristics of the impact response, the simulation model neglecting curing-induced residual stresses predicts a peak force of 5.75 kN, which is approximately 9.7% higher than the experimental value of 5.24 kN. This distinct overestimation arises because ignoring internal stresses causes the numerical model to exhibit an idealized level of structural integrity. However, upon incorporating curing residual stresses, the simulated peak force decreases to 5.36 kN, significantly reducing the error relative to the experimental data to 2.3%. This indicates that residual stresses induce microscopic damage during the early stages of impact or promote interfacial stress superposition around the SMA wires, thereby aligning the structural response more closely with the actual physical conditions.

Secondly, regarding structural stiffness, an analysis of the force–displacement curves reveals that the slope of the loading phase in the model neglecting residual stresses is significantly higher than the experimental value, representing a clear overestimation of stiffness. In contrast, upon the introduction of residual stresses, the curve slope decreases and aligns more closely with the experimental trajectory. This occurs because the SMA wires are primarily under compression within the CFRP matrix; during the impact event, these compressive stresses offset a portion of the applied load. This confirms that the internal stress field generated during curing alters the effective modulus of the composite matrix, thereby enabling a more realistic simulation of the stiffness degradation process.

Figure 17 presents a comparison of the energy–time curves for the SMA-CFRP U-shaped leading edge under low-velocity impact loading. By comparing the experimental data with the two numerical simulation results, the influence of curing-induced residual stresses on the energy absorption characteristics of the SMA-reinforced composite system can be quantitatively evaluated.

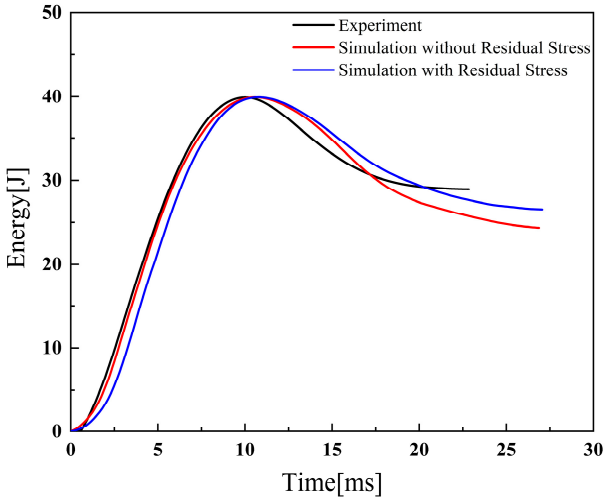


Figure 17. Comparison between experiment and simulation response: the energy–time curve of SMA-CFRP during the impact process.

The experimentally measured final steady-state absorbed energy is 28.9 J. In numerical simulations, the model neglecting residual stresses yields a final energy absorption value of only 24.3 J, representing a high relative error of 18.9%. This discrepancy indicates that ignoring internal stresses leads the model to significantly underestimate the extent of damage evolution within the structure. In contrast, upon the introduction of curing residual stresses, the simulated absorbed energy increases to 26.8 J, with the relative error compared to the experimental value narrowing significantly to 7.8%. This demonstrates that the residual stress field is a critical factor driving irreversible damage and energy

dissipation within the SMA-CFRP structure; incorporating this physical field allows for a more accurate reconstruction of the energy balance during the actual impact process.

A comprehensive comparison between the previously discussed CFRP and the current SMA-CFRP data reveals that residual stresses exert a more pronounced influence on the numerical models of the latter. Due to the significant mismatch in the coefficients of thermal expansion between the SMA wires and the resin matrix, the curing process generates a more extensive residual stress field within the SMA-CFRP. Consequently, when residual stress is neglected, the predictive deviation of the SMA-CFRP simulation model is markedly higher than that of the pure CFRP model. This difference in sensitivity further demonstrates that when studying wire-reinforced composites, accounting for the initial stress state induced by thermal–mechanical coupling is essential for capturing the synergistic effects of phase-transformation energy dissipation and matrix damage.

Compared with previously reported flat SMA-reinforced laminates [6,36], the present U-shaped structure exhibits an additional geometry-dependent effect during impact. In flat laminates, the improvement in impact resistance is mainly associated with the local bridging action, superelastic deformation, and energy dissipation of the embedded SMA reinforcements. In contrast, for the present U-shaped leading-edge component, the curved profile redistributes the impact load and amplifies the role of curing-induced residual stress, especially in the bend–flange transition region. Therefore, the impact response is governed not only by SMA superelasticity and matrix damage, but also by curvature-dependent stiffness distribution and the initial stress concentration introduced during manufacturing. This difference highlights the necessity of considering the thermo-mechanical manufacturing history when evaluating curved SMA-CFRP components.

4. Conclusions

In this study, the low-velocity impact behavior of an SMA-reinforced CFRP U-shaped structure was investigated through a combined experimental and numerical approach, with a particular focus on the influence of curing-induced residual stresses. Based on the comparative analysis of the experimental data and the thermal-mechanical coupled simulation results, the following conclusions can be drawn.

1. Enhancement by SMA Reinforcement.

Experimental results demonstrate that the integration of superelastic SMA wires significantly improves the load-bearing capacity of the U-shaped leading edge, with the peak force increasing by 8.44% compared to pure CFRP. The SMA wires provide a critical bridging effect that suppresses crack propagation and reduces the severity of back-face fiber breakage.

2. Crucial Role of Curing Residual Stresses.

Neglecting curing-induced residual stresses leads to a pronounced overestimation of structural rigidity. By incorporating the thermal-mechanical manufacturing history, the relative errors for peak force and absorbed energy in the SMA-CFRP model were reduced from 9.7% and 18.9% to 2.3% and 7.8%, respectively, validating the necessity of considering initial stress states in hybrid material systems.

3. Residual Stress-Induced Damage Mechanism.

The CTE mismatch between SMA wires and the resin matrix generates significant internal stresses that lower the damage initiation threshold. This facilitates a more realistic simulation of extensive matrix cracking and delamination, aligning the numerical energy dissipation laws with actual physical observations under impact loading.

4. Synergistic Energy Dissipation.

At maximum deflection, the SMA mesh undergoes a complete austenite-to-martensite phase transformation. This superelastic behavior, combined with irreversible matrix dam-

age, forms a synergistic energy dissipation mechanism that enhances the overall impact toughness and facilitates the post-impact shape recovery of the structure.

Overall, the present work establishes a validated thermo-chemo-mechanical framework for predicting the low-velocity impact response of SMA-CFRP curved structures, thereby laying the foundation for broader applications to more complex geometries and service environments. Future work will extend the present thermo-chemo-mechanical framework to other curved and stiffened composite geometries, such as hat-shaped, channel-shaped, and more complex aerospace leading-edge structures. In addition, the coupled effects of environmental and service conditions, including moisture uptake, temperature variation, and repeated impact loading, will be considered to further evaluate the long-term durability and damage tolerance of SMA-CFRP hybrid components.

Author Contributions: Conceptualization, L.W. and Y.X.; methodology, L.W.; software, L.W.; validation, Y.X. and J.W.; formal analysis, S.Z.; investigation, L.W.; resources, Y.X.; data curation, S.Z.; writing—original draft preparation, L.W.; writing—review and editing, J.W.; visualization, L.W.; supervision, Y.X.; project administration, J.W.; funding acquisition, Y.X. and J.W. All authors have read and agreed to the published version of the manuscript.

Funding: This research was funded by the National Natural Science Foundation of China (12220101002, U24A2004, 12372156) and the Shaanxi Provincial Key Science and Technology Innovation Team (2023-CX-TD-14).

Data Availability Statement: The data presented in this study are available from the corresponding author upon reasonable request.

Conflicts of Interest: The authors declare no conflicts of interest.

References

1. Zhang, Z.; Liu, Y.; Tie, Y.; Hou, Y.; Li, C. Self-healing effect on the impact-resistance of hybrid stitch toughening CFRP composites: Experimental and numerical study. *Thin-Walled Struct. Struct.* **2025**, *206*, 112635. [CrossRef]
2. Perera, Y.S.; Muwanwella, R.M.H.W.; Fernando, P.R.; Fernando, S.K.; Jayawardana, T.S.S. Evolution of 3D weaving and 3D woven fabric structures. *Fash. Text.* **2021**, *8*, 11. [CrossRef]
3. Teng, X.; Xu, Y.; Zhang, W.; Liu, W. The use of pre-hole Z-pinning (PHZ) method to improve the impact resistance and post-impact flexural performance of composite skin/stringer joints. *Thin-Walled Struct.* **2022**, *180*, 109909. [CrossRef]
4. Verma, L.; Andrew, J.J.; Sivakumar, S.M.; Balaganesan, G.; Vedantam, S.; Dhakal, H.N. Evaluation of quasi-static indentation response of superelastic shape memory alloy embedded GFRP laminates using AE monitoring. *Polym. Test.* **2021**, *93*, 106942. [CrossRef]
5. Xue, Y.-J.; Wang, W.-W.; Tan, X.; Hui, Y.-X.; Tian, J.; Zhu, Z.-F. Mechanical behavior and recoverable properties of CFRP shape memory alloy composite under different prestrains. *Constr. Build. Mater.* **2022**, *333*, 127186. [CrossRef]
6. Wang, L.; Wang, J.; Xu, Y.; Liu, Y.; Teng, X.; Zhu, J.; Zhang, W. Experiments and simulations on the impact resistance of superelastic shape memory alloy reinforced composites. *Thin-Walled Struct.* **2025**, *210*, 112977. [CrossRef]
7. Ma, H.-L.; Lau, K.-T.; Hui, D.; Shi, S.-Q.; Poon, C.-K. Theoretical analysis on the pullout behavior of carbon nanotube at cryogenic environment with the consideration of thermal residual stress. *Compos. Part B Eng.* **2017**, *128*, 67–75. [CrossRef]
8. Zhang, M.; Zhang, S.; Xie, H.; Li, S. Micromechanical analysis and experimental studies of thermal residual stress forming mechanism in FRP composites. *Appl. Compos. Mater.* **2021**, *28*, 1945–1957. [CrossRef]
9. Huang, G.Q.; Yan, Y.F.; Wu, J.; Shen, Y.F.; Gerlich, A.P. Microstructure and mechanical properties of fine-grained aluminum matrix composite reinforced with nitinol shape memory alloy particulates produced by underwater friction stir processing. *J. Alloys Compd.* **2019**, *786*, 257–271. [CrossRef]
10. Santosh, S.C.; Rao, M. Recent progress in shape memory alloy reinforced composites: A review of the properties, production, mechanisms involved and functional applications. *Mater. Today Proc.* **2024**, *123*, 62–72. [CrossRef]
11. Qian, H.; Umar, M.; Khan, M.N.A.; Shi, Y.; Manan, A.; Raza, A.; Li, F.; Li, Z.; Chen, G. A state-of-the-art review on shape memory alloys (SMA) in concrete: Mechanical properties, self-healing capabilities, and hybrid composite fabrication. *Mater. Today Commun.* **2024**, *40*, 109738. [CrossRef]
12. Fallah, A.; Dehkordi, M.B. A new nonlinear finite element model for transient dynamic response of a micro composite plate embedded with micro SMA wires considering the size effects. *Mech. Adv. Mater. Struct.* **2022**, *29*, 6733–6754. [CrossRef]

13. Jang, B.-K.; Kishi, T. Influence of stacking angle of carbon fibers on fracture behavior of TiNi fiber impregnated CFRP composites. *J. Alloys Compd.* **2006**, *419*, 208–212. [CrossRef]
14. Zhao, S.; Teng, J.; Wang, Z.; Sun, X.; Yang, B. Investigation on the mechanical properties of SMA/GF/epoxy hybrid composite laminates: Flexural, impact, and interfacial shear performance. *Materials* **2018**, *11*, 246. [CrossRef] [PubMed]
15. Wang, Z.; Liu, Y.; Li, H.; Sun, M. Effect of enhancement of interface performance on mechanical properties of shape memory alloy hybrid composites. *Compos. Interfaces* **2018**, *25*, 169–186. [CrossRef]
16. Cohades, A.; Hostettler, N.; Pauchard, M.; Plummer, C.J.; Michaud, V. Stitched shape memory alloy wires enhance damage recovery in self-healing fibre-reinforced polymer composites. *Compos. Sci. Technol.* **2018**, *161*, 22–31. [CrossRef]
17. Karimi, M.; Bayesteh, H.; Mohammadi, S. An adapting cohesive approach for crack-healing analysis in SMA fiber-reinforced composites. *Comput. Methods Appl. Mech. Eng.* **2019**, *349*, 550–575. [CrossRef]
18. Bao, R.; Liu, J.; Xiao, Z.; Joshi, S.C. Thermo-chemo-mechanical modeling of residual stress in unidirectional carbon fiber-reinforced polymers during manufacture. *Materials* **2024**, *17*, 3040. [CrossRef]
19. Zhang, C.; Zhang, G.; Xu, J.; Shi, X.P.; Wang, X. Review of curing deformation control methods for carbon fiber reinforced resin composites. *Polym. Compos.* **2022**, *43*, 3350–3370. [CrossRef]
20. Rashid, I.A.; Shaker, K.; Nawab, Y. Shape distortion in composites: Sources, characterization, and remedies. *Mehran Univ. Res. J. Eng. Technol.* **2023**, *42*, 1–15. [CrossRef]
21. Gonçalves, P.T.; Arteiro, A.; Rocha, N.; Pina, L. Numerical analysis of micro-residual stresses in a carbon/epoxy polymer matrix composite during curing process. *Polymers* **2022**, *14*, 2653. [CrossRef] [PubMed]
22. Zhang, F.; Ye, Y.; Li, M.; Wang, H.; Cheng, L.; Wang, Q.; Ke, Y. Computational modeling of micro curing residual stress evolution and out-of-plane tensile damage behavior in fiber-reinforced composites. *Compos. Struct.* **2023**, *322*, 117370. [CrossRef]
23. Wang, B.; Fan, S.; Chen, J.; Yang, W.; Liu, W.; Li, Y. A review on prediction and control of curing process-induced deformation of continuous fiber-reinforced thermosetting composite structures. *Compos. Part A Appl. Sci. Manuf.* **2023**, *165*, 107321. [CrossRef]
24. Xu, M.; Zhou, R.; Ni, A.; Ding, A. A simple methodology for predicting process-induced spring-in of curved composite parts. *Compos. Commun.* **2022**, *32*, 101158. [CrossRef]
25. Bogetti, T.A.; Gillespie, J.W., Jr. Process-induced stress and deformation in thick-section thermoset composite laminates. *J. Compos. Mater.* **1992**, *26*, 626–660. [CrossRef]
26. Cheng, J.; Xu, Y.; Zhang, W.; Liu, W. A multiscale study on warpage of multi-pinned composites induced by curing process. *Compos. Struct.* **2024**, *333*, 117951. [CrossRef]
27. Littell, J.D.; Binienda, W.K.; Arnold, W.A.; Roberts, G.D.; Goldberg, R.K. Effect of microscopic damage events on static and ballistic impact strength of triaxial braid composites. *Compos. Part A Appl. Sci. Manuf.* **2009**, *40*, 1846–1862. [CrossRef]
28. Zhao, L.G.; Warrior, N.A.; Long, A.C. A thermo-viscoelastic analysis of process-induced residual stress in fibre-reinforced polymer–matrix composites. *Mater. Sci. Eng. A* **2007**, *452*, 483–498. [CrossRef]
29. Wang, X.; Su, H.; Jia, Y.; Li, P. Integrated analysis on cure–microstructure–property–deformation correlation of carbon fiber reinforced resin composites. *Comput. Mater. Sci.* **2015**, *109*, 7–13. [CrossRef]
30. White, S.R.; Hahn, H.T. Process modeling of composite materials: Residual stress development during cure. Part II. Experimental validation. *J. Compos. Mater.* **1992**, *26*, 2423–2453. [CrossRef]
31. Kravchenko, O.G.; Kravchenko, S.G.; Pipes, R.B. Chemical and thermal shrinkage in thermosetting prepreg. *Compos. Part A Appl. Sci. Manuf.* **2016**, *80*, 72–81. [CrossRef]
32. Hashin, Z. Failure criteria for unidirectional fiber composites. *J. Appl. Mech.* **1980**, *47*, 329. [CrossRef]
33. Bogenfeld, R.; Kreikemeier, J.; Wille, T. Review and benchmark study on the analysis of low-velocity impact on composite laminates. *Eng. Fail. Anal.* **2018**, *86*, 72–99. [CrossRef]
34. Mohsin, M.A.A.; Iannucci, L.; Greenhalgh, E.S. Experimental and numerical analysis of low-velocity impact of carbon fibre-based non-crimp fabric reinforced thermoplastic composites. *Polymers* **2021**, *13*, 3642. [CrossRef]
35. Wang, J.; Gu, X.; Xu, Y.; Zhu, J.; Zhang, W. Thermomechanical modeling of nonlinear internal hysteresis due to incomplete phase transformation in pseudoelastic shape memory alloys. *Nonlinear Dyn.* **2021**, *103*, 1393–1414. [CrossRef]
36. Gu, X.; Su, X.; Wang, J.; Xu, Y.; Zhu, J.; Zhang, W. Improvement of impact resistance of plain-woven composite by embedding superelastic shape memory alloy wires. *Front. Mech. Eng.* **2020**, *15*, 547–557. [CrossRef]

Disclaimer/Publisher's Note: The statements, opinions and data contained in all publications are solely those of the individual author(s) and contributor(s) and not of MDPI and/or the editor(s). MDPI and/or the editor(s) disclaim responsibility for any injury to people or property resulting from any ideas, methods, instructions or products referred to in the content.